Rev. Roum. Sci. Techn.– Électrotechn. et Énerg.
Vol. **71**, *3*, pp. 361–366, Bucarest, 2026

PERFORMANCE-ORIENTED DESIGN OF A DUAL-ROTOR AXIAL-FLUX FLUX-REVERSAL MACHINE

HARUN SERHAT GERÇEKCİOĞLU[1]

Keywords: Dual-rotor machine; Axial-flux machine; Torque ripple; Optimization; Finite element analysis (FEA).

This study presents a dual-rotor axial-flux flux-reversal permanent magnet machine (DR-AFFRM) topology, combining a dual-rotor and axial-flux configuration that is not widely documented in the literature. The proposed design innovatively combines an axial-flux configuration with a dual-rotor architecture to enhance torque density while mitigating torque ripple. A finite element model integrated with a genetic algorithm-based optimization framework is employed to optimize critical geometric and magnetic parameters. The optimized design reduces permanent magnet volume by 53.48%, improves efficiency from 81.62% to 84.11%, and delivers an average torque of 106.44 Nm at 1500 rpm. The linear torque–current characteristic confirms effective magnetic utilization without saturation. The results demonstrate that the proposed topology provides a balanced, high-performance solution for high-precision electric-drive applications.

1. INTRODUCTION

Permanent magnet machines are widely adopted due to their high efficiency and compactness. Among them, axial-flux permanent magnet (AFPM) machines are notable for high torque density and short axial length, although thermal, mechanical, and manufacturing challenges remain [1–3]. Within AFPM topologies, flux-reversal permanent magnet (FRPM) machines employ stator-mounted magnets and salient rotors, enabling robust structures and high torque density. However, torque ripple, cogging torque, and reduced power factor remain critical limitations [4–6]. Recent studies report that geometric refinement and multi-objective optimization, particularly GA-based approaches, effectively improve torque behavior and magnet utilization [7–10]. Nevertheless, a systematic investigation of dual-rotor axial-flux FRPM machines remains absent. Motivated by this gap, this study proposes a dual-rotor axial-flux FRPM (DR-AFFRM) topology (Fig. 1) aimed at improving torque smoothness and electromagnetic performance.

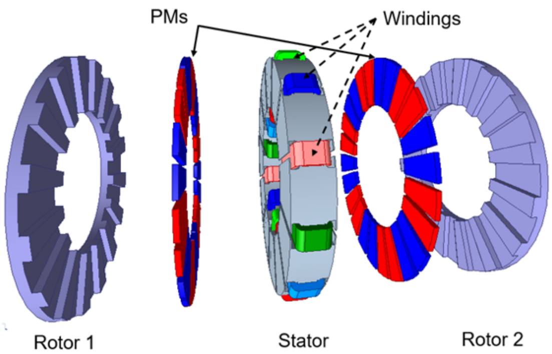

Fig. 1 – Topology of DR-AFFRM machine.

2. OPERATING PRINCIPLE AND DESIGN OF FRM

Flux reversal machines (FRMs) operate through periodic magnetic flux reversal within stator windings, enabled by stator-mounted magnets and salient rotors [11,12]. Depending on rotor position, magnets generate both leakage and main working flux components, with only the latter contributing to the winding linkage. Rotor movement alters the dominant magnet polarity, producing alternating flux linkages and torque.

FRMs are characterized by shared stator magnetic circuits for magnet- and winding-generated fluxes, reducing magnet volume while preserving torque capability. Torque production arises from the doubly salient structure, which combines reluctance and permanent-magnet torque components [13]. Although FRMs offer high torque density and structural simplicity, sharp flux transitions introduce torque ripple and cogging effects [14].

In axial-flux FRMs, the axial-flux orientation shortens magnetic paths and reduces reluctance, thereby improving torque density. Dual-rotor configurations further enhance symmetry, balance axial forces, and increase effective flux linkage [15–17].

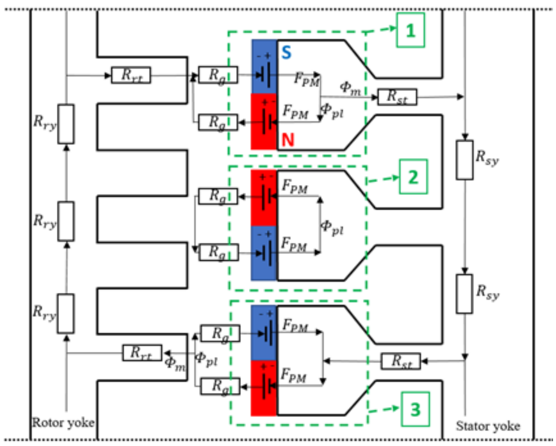

Fig. 2 – The equivalent magnetic circuit of DR AF-FRM.

For each rotor side, the corresponding flux components Φ_{R1} and Φ_{R2} link to the stator windings through two magnetic paths, as illustrated in Fig. 2:

$$\Phi_{R1} = \Phi_{R2} = \Phi_m. \quad (1)$$

Thus, the effective total flux linkage becomes:

$$\Phi_{eq} = \Phi_{R1} + \Phi_{R2} = 2\Phi_m. \quad (2)$$

According to Faraday's law, the phase voltage is expressed as:

$$E_{ph} = N\frac{\mathrm{d}\Phi_{eq}}{\mathrm{d}t} = 2N\frac{\mathrm{d}\Phi_m}{\mathrm{d}t}, \quad (3)$$

These expressions show that a dual-rotor configuration increases both EMF and total flux linkage [18]. Considering the total flux, the electromagnetic torque is given by:

$$T_{2R} = k_t \Phi_{eq} I_q. \quad (4)$$

[1] Tokat Gaziosmanpasa University, Department of Electrical and Electronics Engineering, Türkiye.
E-mail: harun.gercekcioglu@gop.edu.tr

DOI: 10.59277/RRST-EE.2026.3.4

Substituting eq. (2) yields:

$$T_{2R} = 2k_t\Phi_m I_q = 2T_{1R}. \quad (5)$$

In practice, the actual increase is slightly lower due to leakage effects and magnetic cross-coupling. For a dual-rotor system, torque can be expressed as:

$$T_{2R} = \pi k_D k_{\omega 1} B_{mg} A_m D_o^3 \cos\varphi \quad (6)$$

This relationship demonstrates that torque is directly proportional to the cube of the outer diameter and the air-gap flux density [19]. Considering the symmetry of the air gap and the rotor–stator arrangement, the equivalent magnetic reluctance is given by:

$$R_{eq} = \frac{2g}{\mu_0 A_g} + \frac{l_{Fe}}{\mu_{Fe} A_{Fe}}. \quad (7)$$

This reluctance represents the primary limitation on flux production, and dual-rotor symmetry effectively reduces the equivalent reluctance [19]. The relationship between air-gap flux density and magnet thickness is:

$$B_{mg} = \frac{B_r h_{mag}}{h_{mag} + \mu_r g}. \quad (8)$$

The dual-rotor configuration increases B_{mg} by supplying flux from both sides and helps reduce torque ripple [18, 19]. The electromagnetic apparent power is expressed as:

$$S_{elm,2R} = 2\pi^2 k_D k_{\omega 1} n_s B_{mg} A_m D_o^3 , \quad (9)$$

and the average torque is:

$$T_{2R} = \frac{S_{elm,2R}\cos\varphi}{2\pi n_s} = \pi k_D k_{\omega 1} B_{mg} A_m D_o^3 \cos\varphi. \quad (10)$$

These formulations demonstrate that the dual-rotor structure ideally doubles torque production; however, this improvement is moderated by mechanical and magnetic constraints. The symmetric magnetic circuit of the dual-rotor configuration homogenizes flux distribution and reduces torque ripple. By optimizing the air gap and magnet thickness, torque density can be increased by approximately 20–30%. Rotor symmetry also reduces mechanical vibration, supporting stable operation at high speeds [19]. These equations, based on the magnetic circuit approach, enable the determination of key geometric variables such as the outer diameter D_o , inner diameter D_i , pole pitch τ , and air-gap length g , as well as electromagnetic parameters including magnet thickness h_{mag} , air-gap flux density B_{mg} , and line current density A_m [20]. In the initial calculations, the target output power P_{out} , rated speed n_s , and design efficiency η were considered as predefined design constraints, while the remaining parameters were derived analytically. This method, when applied to the dual-rotor FRPM configuration, enables a balanced preliminary design in terms of torque production, flux density, and power density.

Preliminary machine dimensions and electromagnetic parameters were derived analytically using classical axial-flux design equations [20], enabling balanced estimation of torque, flux density, and power density prior to FEA validation. Electromagnetic performance is strongly influenced by slot–pole combinations, which govern flux symmetry and harmonic behavior [21]. In this design, a three-phase DR-AFFRM employing a 12-slot/16-pole configuration was selected due to its favorable winding factor and magnetic loading characteristics. While this configuration provides high torque capability, torque ripple effects are mitigated through subsequent optimization. The geometric and electromagnetic parameters obtained from the preliminary design are summarized in Tables 1 and 2, and are further refined via optimization and finite element analysis.

Table 1

Initial design parameters.

Initial Parameters	Description	Value
V	Voltage	380 V
ω	Speed	1500 rpm
g	Air gap (each air gap)	0.5 mm
N_s	Stator slot number	12
N_r	Rotor teeth number	16
η	Efficiency	% 90
cos φ	Power factor	0.7
$B_{mg}A_m$	Magnetic flux-Electric load	26000 TA/m
q_s	Slot number per phase-per pole	3
J	Current density	6.5 A/mm2
k_{st}	Lamination factor	0.97
k_w	Winding factor	0.97
k_{ill}	Fill factor	0.45
k_d	Stator inner/outer ratio	0.58

Table 2

Initial sizing parameters.

Parameters	Description	Value
D_o	Stator and rotor output diameter	250 mm
D_i	Stator and rotor input diameter	150 mm
b_{s0}	Stator Slot openness width	4 mm
b_{s1}	Stator Slot top width	18 mm
b_{s2}	Stator Slot bottom width	18 mm
h_{s0}	Stator Slot openness height	3 mm
h_{s1}	Stator Slot entrance height	1 mm
h_{s2}	Stator Slot height	18 mm
r_s	Stator Slot bottom wrap	1 mm
τ_1	Stator teeth width	10 mm
W_1	Number of conductors per slot	100
d_{co}	Wire diameter	1 mm
d_r	Wire wrap	0.1 mm
a_1	Parallel branches	1
R_s	Stator resistance	0.79223 ohm
L_{stator}	Stator length	80 mm
L_{rotor1}	Rotor length (Rotor1=Rotor2)	20 mm
h_{mag}	Permanent magnet height	3 mm
τ_{rotor}	Rotor teeth width	12 mm
h_{rotor}	Rotor slot height	10 mm

3. FINITE ELEMENT ANALYSIS (FEA) AND PRELIMINARY RESULTS

The Finite element method (FEM) is a well-established numerical technique for accurately analyzing electromagnetic systems with complex geometries and non-uniform material properties by solving Maxwell's equations. In this study, simulations are conducted using ANSYS Maxwell, an FEM-based low-frequency electromagnetic solver featuring adaptive meshing to capture critical field variations and improve torque prediction accuracy [22, 23].

To ensure precise control of excitation conditions and maintain stable phase current amplitudes independent of impedance variations, current sources are employed instead of voltage sources. The three-phase excitation currents are defined as ideal sinusoidal waveforms, enabling consistent evaluation of the machine's electromagnetic behavior under controlled operating conditions.

The applied three-phase currents follow sinusoidal waveforms, as defined by eqs. (13), (14), and (15). Rotor angular speed Ω_r;

$$\Omega_r = 2\pi\omega/60, \quad (11)$$

$$\Omega_e = \Omega_r N_r, \quad (12)$$

N_r is the number of rotor teeth. Three-phase currents to apply:

$$I_A = I_{max}\sin(\Omega_e t + \beta) \quad (13)$$

$$I_B = I_{max}\sin(\Omega_e t + \beta + 120) \quad (14)$$

$$I_C = I_{max}\sin(\Omega_e t + \beta - 120) \quad (15)$$

where β represents a phase angle parameter that plays a critical role in achieving maximum torque output under a given current excitation. To determine the optimal β value, a parametric sweep of the current angle was conducted on the DR-AFFRM model. The current phase angle was varied from 0^o to 120^o in 10^o increments, and simulations were performed accordingly. The torque output was evaluated for each angle, and the optimal torque was observed at $\beta = 20^o$. The simulations were carried out over a duration corresponding to two electrical periods (0.04 s), employing a time step of 0.0001 s to ensure high temporal resolution. This fine time discretization enables accurate capture of rapid transient variations in current, voltage, and electromagnetic torque, thereby providing reliable results for the evaluation of the DR-AFFRM's dynamic performance. The excitation parameters used in the simulations are summarized in Table 3, and the specific material choices are summarized in Table 4. The simulated torque reached a peak average value of 132.0631 Nm, with a corresponding torque ripple of 55.02%, primarily attributed to the slot–pole interaction and non-uniform air-gap flux distribution. The maximum magnetic flux density (*B*) was observed to reach approximately 2.29 T within localized regions of the stator core, particularly in thinner sections where magnetic saturation tends to occur (Fig. 5). This indicates that the magnetic design operates near the upper limit of the core material's flux capacity. The current density (*J*) attained a value of 6.83 A/mm², which is consistent with the design target range and confirms the effective utilization of the stator winding space while maintaining acceptable thermal loading. These results collectively demonstrate that the designed DR-AFFRM achieves a high torque output at the cost of moderate flux saturation and elevated torque ripple, aspects that are further addressed in the optimization stage. Initial FEM results showed promising torque but notable torque ripple, indicating the need for further optimization. Accordingly, geometric and electromagnetic parameters were systematically refined, with the primary objective of minimizing torque ripple and improving torque smoothness.

Using the baseline design parameters, a two-dimensional finite element (2D-FEM) model of the proposed DR-AFFRM was developed in ANSYS Maxwell to evaluate electromagnetic field distribution and torque characteristics.

Table 3

Excitation parameters.

Parameters	Descriptions	Value
N_r	Rotor teeth number	16
ω	Speed	1500 rpm
Ω_r	$\Omega_r = 2\pi\omega/60$	157.07963 rad/s
Ω_e	$\Omega_e = \Omega_r N_r$	2513.2741 rad/s
I_{max}	Current	30 A
β	Current angle	20^o
I_{rms}	Current (rms)	21.2132 A (rms)

Using the baseline design parameters, a two-dimensional finite element (2D-FEM) model of the proposed DR-AFFRM was developed in ANSYS Maxwell to evaluate electromagnetic field distribution and torque characteristics. Although three-dimensional (3D) modeling provides higher geometric accuracy, the 2D approach was adopted to significantly reduce computational cost while preserving the essential magnetic coupling between the stator and dual rotors [24]. Comparative analysis showed that the average torque deviation between 2D and 3D models remained within approximately 4% (Fig. 3), indicating that the 2D model is sufficiently accurate for preliminary performance evaluation and parametric studies, with 3D simulations reserved for final verification. Figure 4 illustrates the initial geometric parameters of the DR-AFFRM, including stator diameters, rotor dimensions, and magnet thickness, which define the baseline design and subsequent optimization variables. FEA was conducted at a maximum excitation current of 30 A to evaluate the electromagnetic performance of the proposed DR-AFFRM.

Table 4

Materials.

DR-AFFRM parts	Materials
Stator	JFE_Steel_50JN1000
Rotor	JFE_Steel_50JN1300
Magnets	Magfine_NdFeB30

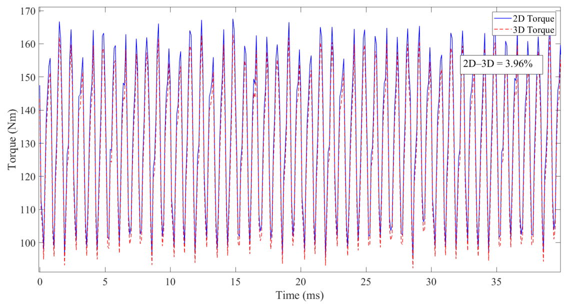

Fig. 3 – Figure 3. Comparison of 2D and 3D torque analysis.

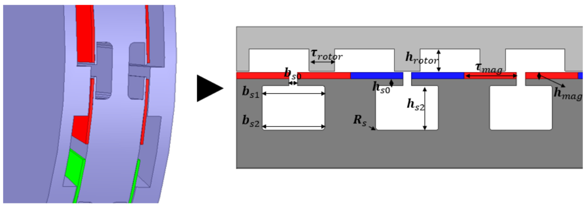

Fig. 4 – Initial model of DR-AFFRM.

4. OPTIMIZATION AND PERFORMANCE RESULTS

Genetic algorithms (GAs) are effective optimization techniques in electrical machine design, particularly for torque ripple mitigation and performance enhancement. Accordingly, a GA-based approach was adopted to explore the DR-AFFRM design space.

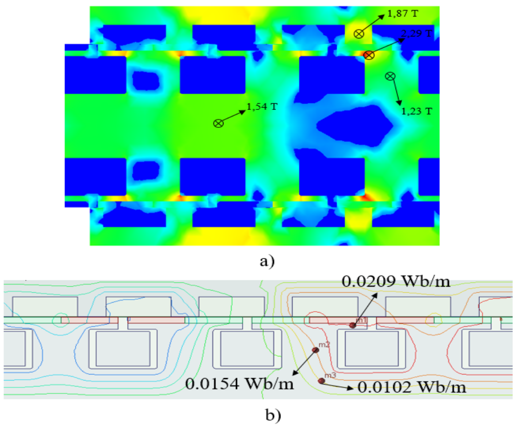

Fig. 5 – Initial model a) magnetic flux density (*B*) b) flux lines (*A*)

Candidate solutions were initialized using physically feasible parameters. Individuals were evaluated via a multi-objective fitness function incorporating average torque, torque ripple, efficiency, and magnetic losses. Standard operators—selection, crossover, and mutation—were applied to maintain diversity, and the optimization was terminated upon satisfying predefined performance criteria. [25,26]. The dual-rotor AF-FRM is optimized using ten critical geometric variables (Table 5), where the GA minimizes torque ripple while maintaining torque capability. The cost function evolution is presented in Fig. 6, and the optimized parameters are summarized in Table 6.

Table 5

Optimization parameters.

Optimization number	Parameters	Description
Opt 1	b_{s0}	Stator slot opening (mm)
Opt 2	b_{s1}	Stator slot top width (mm)
Opt 3	b_{s2}	Stator slot bottom width (mm)
Opt 4	h_{s0}	Stator teeth height (mm)
Opt 5	h_{s2}	Stator slot height (mm)
Opt 6	R_s	Stator slot bottom fillet (mm)
Opt 7	τ_{rotor}	Rotor teeth width (emb.)
Opt 8	h_{rotor}	Rotor slot height (mm)
Opt 9	τ_{mag}	Magnet width (emb.)
Opt 10	h_{mag}	Magnet height (mm)

The optimization outcomes reveal significant improvements in the electromagnetic behavior of the DR-AFFRM through parameter adjustments guided by the genetic algorithm (GA). Each optimized pair of design variables contributed to torque ripple improvement through geometric and magnetic flux redistribution mechanisms, as detailed below and as shown in Fig. 7–11.

The optimization process introduced coordinated geometric modifications that collectively improved flux distribution and torque smoothness. Adjustments in stator slot widths reshaped the tooth-root flux paths, alleviating local saturation and reducing low-order harmonics, which contributed to torque ripple suppression despite a partial reduction in flux per pole. Simultaneous refinement of rotor tooth and magnet widths enhanced flux continuity and minimized saturation effects, enabling smoother air-gap flux transitions. Reductions in stator and rotor slot heights decreased axial leakage flux and airgap permeance variability, further stabilizing the electromagnetic torque waveform. Additionally, slight decreases in stator tooth and magnet heights lowered flux concentration, mitigating saturation-driven ripple components. Enlarged slot openings and fillet radii improved flux dispersion at tooth tips and roots, reducing cogging torque and local field distortions. Although these changes slightly reduced average torque, they significantly enhanced magnetic material utilization and torque quality by producing a more uniform air-gap flux distribution.

Table 6

Optimization results.

Optimization number	Initial Value	Optimization range Min.	Optimization range Max.	Optimization results
Opt 1	4	1	15	10.13533
Opt 2	24	24	40	24.84162
Opt 3	24	24	40	38.72178
Opt 4	3	1	3.5	2.73102
Opt 5	20	18	25	18.41398
Opt 6	3	3	5	4.90627
Opt 7	0.5	0.1	0.9	0.68008
Opt 8	15	5	18	5.06004
Opt 9	0.5	0.4	0.7	0.40734
Opt 10	2.1	2	2.95	2.11258

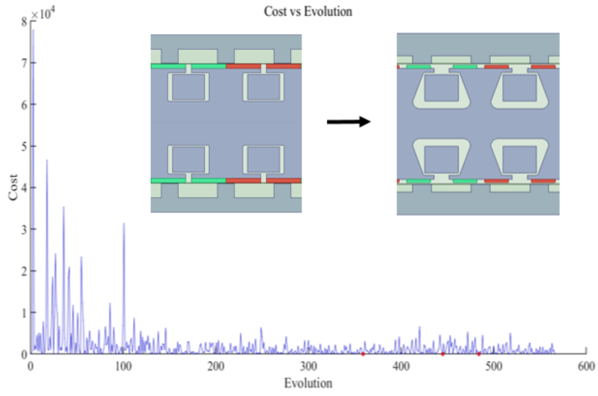

Fig. 6 – Costs vs evolution.

The magnetic flux density was evaluated both before and after the optimization process to assess the impact of geometric adjustments on flux distribution. Following optimization, the corresponding values were reduced to 1.89 T, 1.67 T, 1.46 T, and 1.57 T, respectively (Fig. 12).

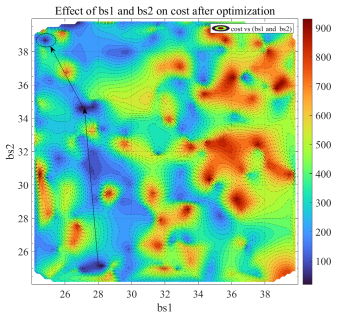

Fig. 7 – Costs vs b_{s1}-b_{s2}.

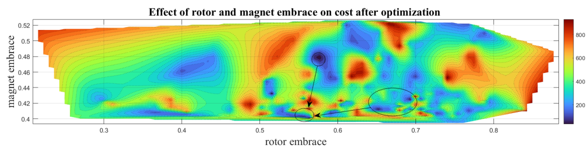

Fig. 8 – Costs vs $\tau_{rotor} - \tau_{mag}$.

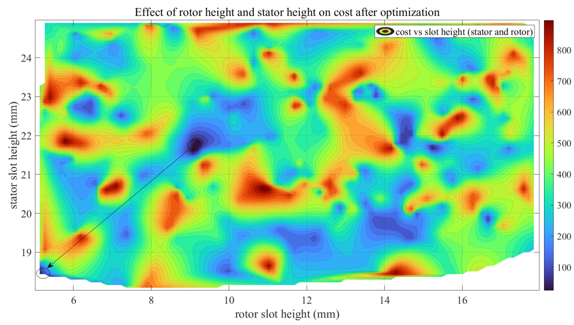

Fig. 9 – Costs vs $h_{s2} - h_{rotor}$.

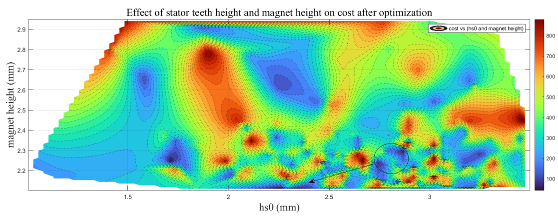

Fig. 10 – Costs vs $h_{s0} - h_{mag}$.

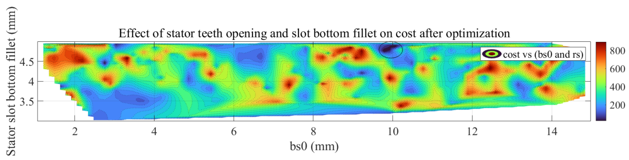

Fig. 11 – Costs vs $b_{s0} - R_s$.

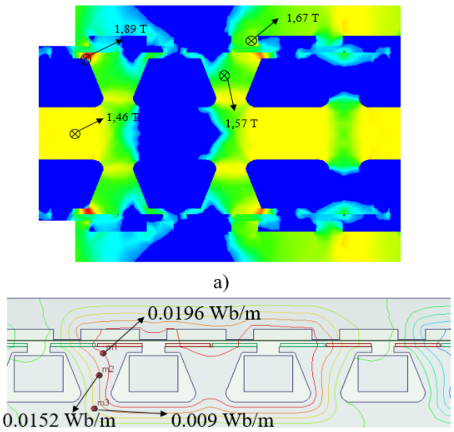

b)

Fig. 12 – Optimized model: a) magnetic flux density (B), b) flux lines (A).

The proposed DR-AFFRM machine was analyzed to assess both its torque performance and energy efficiency under baseline and optimized configurations (Table 7). Initially, the machine operated at 1,500 rpm with a line voltage of 380 V, phase resistance of 0.792 Ω, and phase inductance of 2.425 mH, delivering an average torque of 138.63 Nm with an efficiency of 81.62%. Following a GA-based multi-parameter optimization, primarily targeting a reduction in torque ripple from 55.03% to 10.47% (Fig. 13), the optimized design produced an average torque of 106.44 Nm and achieved an efficiency of 84.11%.

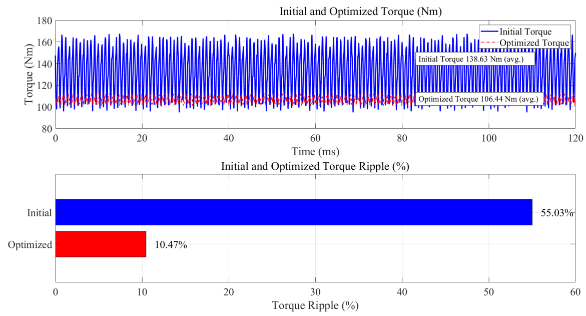

Fig. 13 – Torque and torque ripple results

The reduction in average torque reflects the inherent trade-off of torque ripple improvement, yet the dual-rotor architecture maintained balanced magnetic loading and a homogeneous flux distribution. Torque density, representing torque per unit active machine volume, decreased from approximately 36.8 kNm/m^3 to 28.2 kNm/m^3, reflecting the volumetric impact of prioritizing torque ripple minimization during the optimization process. Concurrently, the torque per permanent-magnet volume T/V_{PM} metric was re-evaluated for both configurations. In the baseline design, this value was approximately $7.6x10^5$ Nm/m^3, whereas in the optimized model it increased to nearly$10.1x10^5$ Nm/m^3. Despite the reduction in average torque, the reported 33% improvement indicates substantially more efficient utilization of magnetic material, demonstrating a more favorable balance between electromagnetic performance and magnet volume. The optimized design also exhibits improved torque smoothness, confirming the effectiveness of GA-based parameter optimization in DR-AFFRMs, consistent with recent findings emphasizing the influence of magnet geometry on torque quality [27, 28].

The torque–current characteristics (Fig. 14) remain nearly linear over the 10–30 A range, indicating the absence of magnetic saturation. Although the optimized machine produces lower torque, the slope of the torque–current curve is preserved, with linear regression yielding approximately 2.72 Nm/A, confirming unchanged torque-per-ampere capability and efficient operation across the tested range.

Table 7

DR-AFFRM initial and optimized performance results.

Parameters	Initial	Optimized
Torque ripple (%)	55.03	10.47
Torque (Nm)	138.63	106.44
Efficiency (%)	81.62	84.10
Torque density (kNm/m^3)	36.8	28.2
$\boldsymbol{T/V_{PM}}$ **(10^5Nm/m^3)**	7.6	10.1

The cogging torque characteristic is typically quantified using a normalized metric defined as the percentage ratio between the peak-to-peak cogging torque amplitude and the machine's average torque [28], expressed as:

$$CT_{\%} = \frac{T_{cog,p-p}}{T_{avg}} \times 100. \quad (16)$$

For the baseline DR-AFFRM, the normalized cogging torque was 43.4%, with a peak-to-peak value of approximately 60.2 Nm relative to the average torque (138.63 Nm), reflecting the strong magnet–stator interaction inherent to flux-reversal topologies.

Following optimization, the normalized cogging torque was reduced to 12.0%, with a peak-to-peak value of 10.39 Nm and an average torque of 106.44 Nm. This represents an approximately 72% improvement, confirming that the optimization strategy effectively suppresses cogging torque by enhancing magnet–tooth alignment and air-gap flux uniformity. Consequently, the optimized machine exhibits significantly smoother no-load torque behavior (Fig. 15).

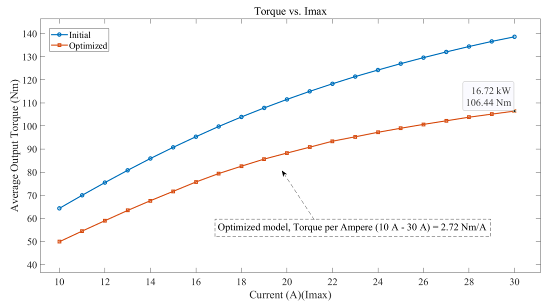

Fig. 14 – Torque vs. current results.

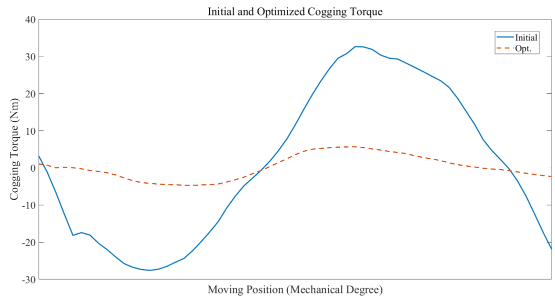

Fig. 15 – Initial and optimized cogging torque.

6. **CONCLUSIONS**

This study validates the proposed dual-rotor axial-flux flux-reversal permanent magnet machine (DR-AFFRM) as a technically viable and scientifically novel topology for high torque-quality applications. The integration of finite element analysis with genetic algorithm-based optimization enabled a substantial reduction in torque ripple, improved efficiency, and more effective permanent-magnet utilization. The optimized design achieved approximately an 81% reduction in torque ripple while maintaining linear torque–current behavior and mitigating magnetic saturation through enhanced flux uniformity. From an engineering perspective, the DR-AFFRM topology exhibits strong potential for precision-oriented and vibration-sensitive drive systems, including servo drives and electric mobility platforms. The presented optimization framework is systematic and transferable to other axial-flux and multi-rotor machine structures. Future work will emphasize full three-dimensional modeling, prototype development, experimental validation, and expanded multi-objective optimization incorporating thermal, acoustic, and cost constraints.

CREDIT AUTHORSHIP CONTRIBUTION STATEMENT

The author carried out the literature review, model development and simulations, analytical calculations, performance and magnetic analyses, evaluation and interpretation of the results, and the writing and compilation of the manuscript.

Received on 22 December 2025

REFERENCES

1. J. Miao, X. Li, L. Jing, Y. Gao, "A novel flux-reversal permanent magnet machine with low torque ripple characteristic," Energies, **18**, *18*, pp. 4834 (2025).
2. H.-J. Kim, S.-W. Baek, "Multi-objective optimal design of an axial flux permanent magnet motor for in-wheel drive considering torque ripple reduction," Energies, **18**, *18*, pp. 4936 (2025).
3. L. Xie, Z. Xu, P. Su, Y. Li, L. Chang, "Harmonic design and optimization of axial-modular flux-reversal permanent-magnet machine," J. Magn., **30**, *1*, pp. 55–66 (2025).
4. L. Jia, M. Lin, P. Wang, "Design, analysis and implementation of a low cogging torque axial-flux PM machine with dual rotors and modular stators for electric vehicles," Energy, **338**, pp. 138760 (2025).
5. A. Boulayaoune, A. Oubelaid, A. Chibah, "Comparative study of inner and outer rotor flux reversal permanent magnet machine for direct drive wind turbine," Rev. Roum. Sci. Techn. – Électrotechn. Et Énerg., **69**, *2*, pp. 123–128 (2024).
6. Z. Ran, Z.-Q. Zhu, D. Liang, "Comparative study of dual-rotor permanent magnet machines with series and parallel magnetic circuits," World Electr. Veh. J., **16**, *1*, pp. 12 (2025).
7. P. Srikhumphun, P. Seangwong, J. Jongudomkarn, A. Siritaratiwat, N. Fernando, S. Somkun, P. Khunkitti, "Design optimization and comparative study of skewed Halbach-array magnets TORUS axial-flux permanent magnet motors for electric vehicles," IEEE Access, **12**, pp. 99912–99920 (2024).
8. L. Xiaolian, J. Libing, "Analysis and optimization of a novel flux reversal PM machine with auxiliary teeth and PM chamfer," J. Electr. Eng. Technol., **20**, *4*, pp. 2191–2200 (2025).
9. F. Pranjić, P. Virtič, "Cogging torque reduction techniques in axial flux permanent magnet machines: a review," Energies, **17**, *5*, pp. 1089 (2024).
10. M. Bharathi, O. C. Sekhar, S. Lakhimsetty, "Performance evaluation of flux reversal machines with rare-earth and non-rare earth excitations for micro wind energy," Curr. Appl. Phys., **80**, pp. 51–63 (2025).
11. I. Shuaibu, E. H. T. Wei, R. Kannan, Y. A. Samaila, "Advancements in axial flux permanent magnet machines utilizing coreless technology: a systematic review," Ain Shams Eng. J., **15**, pp. 103091 (2024).
12. S. Tang, Y. Xu, C. He, J. Yang, "A high torque density dual-stator flux-reversal machine with multiple poles Halbach excitation on outer stator," Actuators, **13**, *8*, pp. 275 (2024).
13. S.-W. Song, W.-H. Kim, "Design and analysis of torque ripple reduction in low-pole axial flux motor," Processes, **13**, *9*, pp. 2913 (2025).
14. J. Asama et al., "Torque ripple reduction of an axial-flux permanent magnet motor with distributed winding," Proc. IEEE IEMDC, Miami, FL, USA, pp. 1–6 (2025).
15. A. Patel, "Cogging torque reduction of axial flux permanent magnet brushless DC motors for electric vehicle applications with magnet segmentation technique," Pamukkale Univ. Muh. Bilim. Derg., **31**, *6*, pp. 977–983 (2025).
16. T. I. Ichim, O. V. Craiu, "Comparison of two bi-phase hybrid stepper motors, one with a solid and the other with a laminated stator," Rev. Roum. Sci. Techn. – Électrotechn. Et Énerg., **70**, *2*, pp. 181–186 (2025).
17. V. Ballestín-Bernad, G. Sanz-Sánchez, J. S. Artal-Sevil, J. A. Domínguez-Navarro, "Analytical modeling of an ironless axial flux machine for sizing purposes," Electronics, **14**, *14*, pp. 2901 (2025).
18. H. Wang, X. Zeng, J. F. Eastham, X. Pei, "Axial flux permanent magnet motor topologies: magnetic performance comparison," Energies, **17**, *2*, pp. 401 (2024).
19. A. G. Yetgin, M. M. Tezcan, "Effect of the lambda parameter on three-phase induction motor design by analytical and magnetic methods," Rev. Roum. Sci. Techn. – Électrotechn. Et Énerg., **70**, *4*, pp. 435–440 (2025).
20. H. Yousefi Javid, A. Yousefi Javid, "Modelling and simulation of a novel axial flux permanent magnet hysteresis motor comparing different disc structures," IET Electr. Power Appl., **19**, *1*, pp. e70008 (2025).
21. T. Tudorache, "Finite element analysis of a flexible dual-speed salient pole synchronous machine," Rev. Roum. Sci. Techn. – Électrotechn. Et Énerg., **70**, *1*, pp. 21–26 (2025).
22. S. M. Oh, K. Akatsu, D. W. Lee, H. J. Lee, "On the iron loss reduction design improvement of an axial flux permanent magnet motor," Actuators, **14**, *12*, pp. 595 (2025).
23. ***ANSYS Inc., *ANSYS Maxwell – Electronics Simulation Software* (2025).
24. H. Liu, J. Tian, G. He, X. Li, "A permanent-magnet eddy-current loss analytical model for axial flux permanent-magnet electric machine accounting for stator saturation," Energies, **18**, *10*, pp. 2462 (2025).
25. E. MacRae et al., "Genetic algorithm-based approach for torque control and increased efficiency across an optimized speed range in switched reluctance drives," IET Electr. Power Appl., **18**, *12*, pp. 1818–1832 (2024).
26. C. Wang et al., "Multi-objective optimization approach for permanent magnet machine via improved soft actor–critic based on deep reinforcement learning," Expert Syst. Appl., **264**, pp. 125834 (2025).
27. J. W. Goh, S. Xie, H. Wang, S. Zhu, K. Yu, C. H. Lee, "Development of a surface-inset permanent magnet motor for enhanced torque density in electric mountain bikes," Energies, **18**, *14*, pp. 3709 (2025).
28. T. Zhou, Z. Xiao, Z. Lian, "Research on torque characteristics of dual-rotor permanent magnet motor and its parameter influence law under magnetic-thermal coupling," Therm. Sci. Eng. Prog., **59**, pp. 103254 (2025).
29. D. Yan, Y. Yan, Y. Cheng, L. Guo, T. Shi, "Research on cogging torque reduction method for permanent magnet synchronous motor accounting for the magnetic pole edge effect," IET Electr. Power Appl., **18**, *1*, pp. 64–75 (2024).